Journal of Alloys and Compounds 896 (2022) 162971

Contents lists available at ScienceDirect

Journal of Alloys and Compounds

journal homepage: www.elsevier.com/locate/jalcom

Abnormal resistive switching in electrodeposited Prussian White thin films

F.L. Faita[a], L.B. Avila[b], J.P.B. Silva[c], M.H. Boratto[d], C.C. Plá Cid[b], C.F.O. Graeff[d], M.J.M. Gomes[c], C.K. Müller[e], A.A. Pasa[b,*]

[a] Instituto de Física, Universidade Federal do Rio Grande do Sul, 91501-970 Porto Alegre, Brazil
[b] Departamento de Física, Universidade Federal de Santa Catarina, 88040-900 Florianópolis, Brazil
[c] Centre of Physics of Minho and Porto Universities (CF-UM-UP), Campus de Gualtar, 4710-057 Braga, Portugal
[d] São Paulo State University (UNESP), School of Sciences, POSMAT - Post-Graduate Program in Materials Science and Technology, 17033-360 Bauru, SP, Brazil
[e] University of Applied Sciences Zwickau, Faculty of Physical Engineering/Computer Sciences, 08056 Zwickau, Germany

ARTICLE INFO

Article history:
Received 21 September 2021
Received in revised form 24 November 2021
Accepted 25 November 2021
Available online 27 November 2021

Keywords:
Prussian White
Resistive switching
Electrodeposition

ABSTRACT

Prussian White (PW) layers were deposited on Au/Cr/Si substrates by electrodeposition and characterized by different techniques. Scanning electron microscopy (SEM) images and Raman mapping reveal a uniform and homogeneous deposit while scanning transmission electron microscopy (STEM) images disclose the grain boundary pattern and the thickness of 300 nm of the PW layer. Resistive switching (RS) effect with an ON/OFF ratio of about 10^2 was observed. The RS mechanism was investigated from the log-log current-voltage plots. Ionic conduction was observed with an activation energy of 0.4 eV that could be associated with potassium ions as possible charge carriers at the grain boundaries. The endurance characteristics were investigated and a stable abnormal RS was observed for consecutive 500 cycles. Moreover, the retention was also evaluated and the high resistive state (HRS) and low resistive state (LRS) were stable up to 1000 s.

1. Introduction

The biggest challenges facing the microelectronic memory industry today are the requirements of less power consumption, less latency, higher density, higher bandwidth, and lower cost, which are leading to the development of alternatives such as resistive switching random access memories (ReRAMs) [1–4]. ReRAMs technology is based on memristors (memristive devices) and is considered as a potential candidate for the next generation of memories since they offer high switching speed, simple cell structure, small cell size, high durability, and multistate switching with potential application in neuromorphic computational systems [5–7].

Memristors have usually the same stack structure as a capacitor with bottom and top electrodes with an intermediate layer, the dielectric, which in this case undergoes a switching in resistance under the action of an applied electric field that defines ON and OFF states due to the formation or rupture of conducting filaments or paths. Different switching behaviors have been observed and classified into two main groups according to their I–V hysteresis loop, namely, unipolar and bipolar. Unipolar switching only depends on the amplitude of the applied voltage and, on the other hand, bipolar switching depends only on the polarity of the applied voltage [8,9]. However, switching hysteresis loops classified as abnormal [10–15], threshold [16–18], and antipolar or complementary [9,19–21] were also described in the literature.

We will describe the resistive switching (RS) results obtained with potassiated Prussian White electrodeposited layers. Prussian White (PW) is an iron hexacyanoferrate with general formula $A_2Fe[Fe(CN)_6]$, where A is an alkaline metal. PW is an abundant and low toxicity material with potential application in sustainable cathodes for batteries [22–26]. Electrodeposited PW layers have been prepared by our group on Au surfaces with cubic or a mixture of cubic and rhombohedral phases, depending on the applied deposition potential, with an average lattice parameter of 10.06 Å [27].

In this work, the observed switching mechanism for PW was the abnormal one. It occurs in switching cells with oxides as TiO_2 [10], ZnO [11,15], $SrTiO_3$ [12], and $GaO_{1.3}$ [13], and no reports were found for ferrocyanides and ferricyanides (Prussian Blue and analogs). In all these intermediate oxide layers, the switching is explained by the presence of oxygen vacancies. The abnormal mechanism displays I–V loops with set and reset switching occurring under the same voltage polarity. It resembles the antipolar or complementary

* Corresponding author.
E-mail address: andre.pasa@ufsc.br (A.A. Pasa).

https://doi.org/10.1016/j.jallcom.2021.162971
0925-8388/

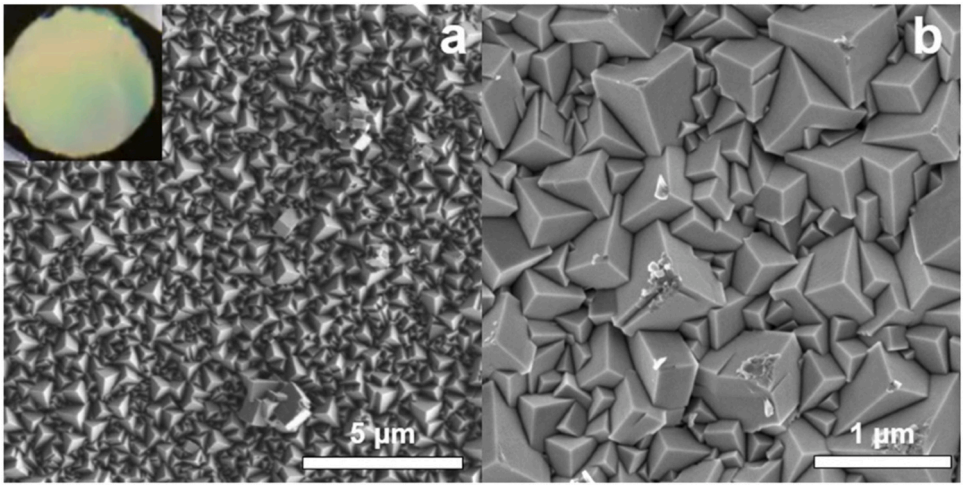

Fig. 1. FEG-SEM images of electrodeposited PW film grown at 0.1 V: (a) Surface overview and photograph image of the film (inset), and (b) Detailed view of the film surface.

resistive switching with the exception that the set voltage is close to zero and that the reset occurs when the voltage sweep is returning from its maximum value. As the abnormal cycle is similar to the complementary loop, Prussian White devices could be an alternative solution for the recurrent cross-talk interference due to sneak-path currents from neighboring memristors [28,29]. In addition, Prussian White can be grown by electrochemical methods that are adequate for large-scale production in the microelectronic industry. In previous work on electrodeposited Prussian Blue layers, a different switching mechanism was observed. Highly reproducible bipolar loops with a switching ratio of about three orders of magnitude were measured [30].

2. Experimental procedures

2.1. Materials preparation

The electrochemical deposition of the PW films was performed in potentiostatic mode in an Ivium CompactStat electrochemical workstation, at room temperature, by using Au/Cr/Si substrates as working electrodes, a Pt foil as the counter electrode, and a saturated calomel electrode (SCE) as reference. All the voltages in the text refer to this reference electrode. The working electrode was prepared by evaporating 50 nm Au on 5 nm Cr on (100) Si substrates with a size of 1 cm × 1 cm at a base pressure of 10^{-7} Torr. The electrodeposition of PW occurred in a circular area of 0.5 cm^2 defined by a mask of adhesive tape on the surface of the working electrode. As electrolyte for the electrochemical synthesis it was used a solution containing 0.25 mM $K_3Fe(CN)_6$, 0.25 mM $FeCl_3$, 1.0 M KCl and 5.0 mM HCl at pH 2.2 [31]. The PW layers were deposited by applying a constant potential of + 0.1 V and limiting the electrodeposited charge to 30 mC.

2.2. Characterization

The PW film morphology was investigated with a TESCAN field emission scanning electron microscope (FEG-SEM, TESCAN Amber) at 2 kV. The SEM was equipped with a focus ion beam (FIB) for cross-section analysis of the films. A film lamella was prepared by FIB and analyzed at 30 kV. In addition, the PW homogeneity in the layer was analyzed by Raman and SEM (RISE) microscopy in a Raman spectrometer (WITec RISE) in combination with an SEM (Zeiss Sigma 300). Raman spectra were obtained using a laser excitation wavelength of 532 nm at a power of 1 mW. The spectra were taken from a PW film area of 15 µm x 15 µm (100 ×100 pixels, with 0.1 s integration time per pixel). In parallel, the surface morphology of the same surface region was imaged by SEM operating at 1 kV.

X-ray photoelectron spectroscopy (XPS) was carried out with a Thermo Scientific K-Alpha using a monochromatic Al kα source and a spot size of 400 µm. The XPS system was equipped with an Ar-ion-sputtering source for depth analysis of the films. XPS spectra were analyzed using Casa XPS software (v. 2.3.23) and calibrated using the reference signal C1s peak position at 284.6 eV [32]. To compare with XPS data, energy-dispersive spectroscopy (EDS) was measured in the FEG-SEM microscope.

For the electrical characterization (current vs voltage (I-V)) was used a Keithley 617 programmable electrometer. The 2 - point probe measurements were done with a bottom electrode (BE), the Au film from the Au/Cr/Si substrate, and a top electrode (TE), a spring test probe with a pointed head of Rh. For measurements at temperatures up to 100 °C, the samples were heated on a hot plate in the air.

3. Results and discussion

3.1. Morphological and structural characterization

Fig. 1 shows typical SEM images of the surface of PW films grown at 0.1 V with a deposited charge of 30 mC. In general, the films appear homogeneous and compact throughout the whole substrate (Fig. 1(a) and inset). The PW is highly crystalline with pyramids on the surface indicating the [111] preferential orientation, as previously reported [27]. Fig. 1(b) illustrates the presence of PW grains on the surface with different sizes, from 100 to 600 nm.

Fig. 2 presents the cross-sectional images of the PW samples prepared with FIB observed in the STEM (scanning transmission electron microscopy) mode. From the images, an average film thickness of about 300 nm can be verified. However, due to the preparation of the lamella by FIB, the images are diffuse and the contrast between the crystalline grains is not so evident. From the subtle contrast at the grain boundaries, we assume the nucleation of small grains on the Au electrode and the subsequent growth of some of these grains to form the compact layer seen in the figure. This nucleation and growth process was previously observed for the electrodeposition of PW and PB on Au surfaces [27,30].

Fig. 3 shows the Raman mapping, taken from the surface (Fig. 3(a)) and bulk (b). The images show a homogeneous distribution of PW (blue color) on both surface and bulk. Additionally, a small amount of Prussian Blue can be identified as shown in red. The corresponding Raman spectrum of the film in Fig. 3(c) clearly shows peaks of the CN stretching bands between 2150 and 2050 cm^{-1}

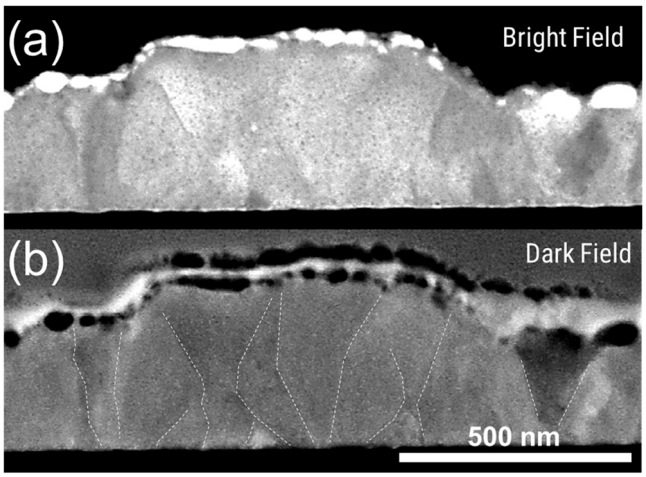

Fig. 2. Scanning transmission electron microscopy images taken from the FIB lamella of the PW films: (a) bright-field and (b) dark-field images. The dashed lines in the dark field image reinforce the grain boundaries close to the electrode surface and along with the thickness of the layer.

coordinated to iron ions. The main peak appears at 2086 cm^{-1} and refers to CN stretching vibration of the [Fe(II),Fe(II)] state [33–35]. The peak at 2124 cm^{-1} is characteristic of CN stretching in [Fe(II),Fe(II)] and [Fe(II),Fe(III)] environments [36] indicating the presence of different forms of PW [37], namely sPW (soluble) and iPW (insoluble) with formulas $K_2Fe[Fe(CN)_6]$ and $K_4Fe_4[Fe(CN)_6]_3$. Other characteristic PW peaks are found at lower wavenumbers. Between 450 and 620 cm^{-1} the peaks are assigned to Fe-C stretching vibrations of the lattice, and at the lower spectral window (200 – 350 cm^{-1}) with a strong peak at 276 cm^{-1} assigned to Fe-CN-Fe bond deformation vibrations [38].

XPS was performed to investigate the elemental composition of the PW thin films at the surface. Fig. 4(a) shows the signals present in the survey spectrum corresponding to the elemental composition of 17 Fe, 29.4 K, 26.6 C, 26.5 N, and 0.5 O, in atomic percentages (at%). The significant amount of K is clear evidence of the accumulation of this element at the surface given that much lower concentrations are expected for the sPW and iPW compounds of 12.50 and 8.51 at%, respectively. The amount of Fefound by XPS is slightly higher than the expected ones for sPW and iPW of 12.50 and 14.89 at%, respectively. However, a small amount of iron may be present in the oxide form since a small amount of oxygen was also detected. For CN ligands, the surface composition indicates a stoichiometric ratio, besides the fact that values around 26 at% are lower than the expected ones for PW of 38 at%, and this is due to the excess of K at the surface.

Fig. 4(b) shows the Fe2p XPS spectrum and fittings. In the energy range of $Fe2p_{3/2}$ and $Fe2p_{1/2}$ states the fitting clearly shows the coexistence of Fe^{2+} (708.9 eV and 722.1 eV) and Fe^{3+} (711.9 eV and 725.1 eV)with a constant energy separation between the Fe2pstates of 13.2 eV [32]. These results are consistent with the Raman measurements to confirm the predominance of the PW phase over the PB one, i.e. more Fe^{2+} ions were detected than Fe^{3+}. Bulk concentration values for the Prussian White sample were obtained using the EDS detection system of 12.6 Fe, 11.3 K, 36.5 C, 36 N, and 3.6 at % O, which were consistent with the electrodeposition of Prussian White with the predominance of the soluble phase.

3.2. Electrical characterization

In Fig. 5(a), we show the room temperature I-V curve of PW with the 1st resistive switching cycle. The PW sample was submitted to a varying potential starting at − 0.60 V and returning at + 0.55 V where a characteristic pinched hysteresis loop is observed, as described by L. Chua for memristors [39]. The device is initially in the low-resistance state (LRS) and switches to the high-resistance state (HRS) at about − 0.50 V (V_{RESET}), and by crossing the zero bias to positive voltage values it switches back to the LRS state, i.e, V_{SET} is positive and close to 0 V. For the returning sweep the switching sequence is very similar to the forward one with V_{RESET} at 0.45 V and V_{SET} negative and also very close to 0 V. A behavior that is classified as abnormal resistive switching [10–15]. In Fig. 5(b) are shown the 1st, 10th, 25th 50th, 100th, 200th, and 500th loops in the semi-log scale with the switching sequence indicated by the arrows. In this figure, one can easily observe that (i) close to zero bias the device switches abruptly to LRS, (ii) the switching in current is about 2 orders of magnitude, and (iii) the superposition of the curves after 500 cycles testify the high stability of the device after a long period of cycling. These measurements were done without external limiting of the maximum current, i.e., without applying a compliance current (CC). To better describe the abnormal bipolar RS behavior several I-V curves were measured under different maximum and starting

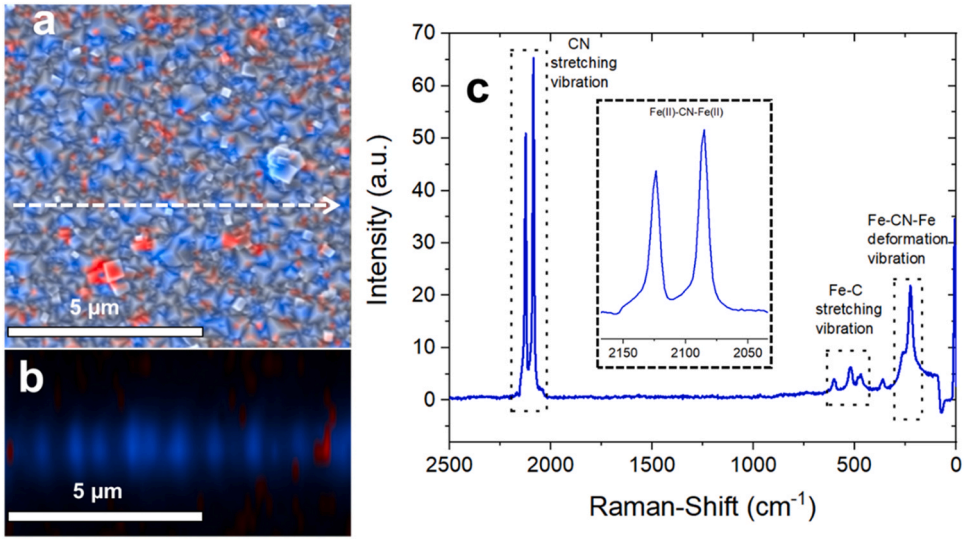

Fig. 3. Raman imaging and spectroscopy of PW thin films electrodeposited with 30 mC at + 0.1 V. (a) Raman scanned area with 15 × 15 μm^2 (blue color) combined with the SEM image of the same sample area. (b) Raman depth scan along the marked white arrow in the image (a). (c) Typical Raman spectrum corresponding to the blue-colored regions of images (a) and (b).

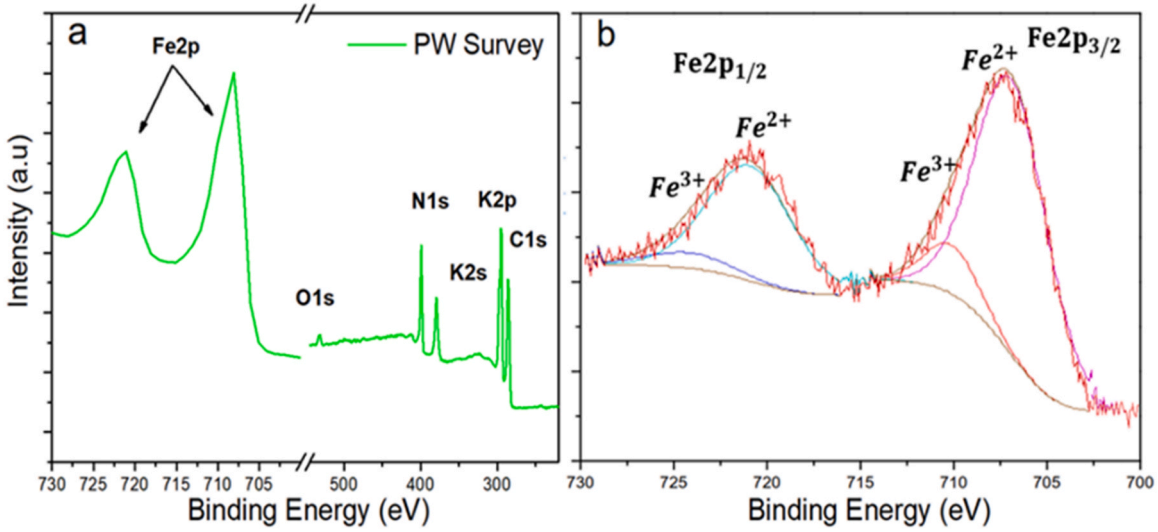

Fig. 4. (a) XPS survey spectrum of the PW film, and (b) core level spectrum of Fe2p.

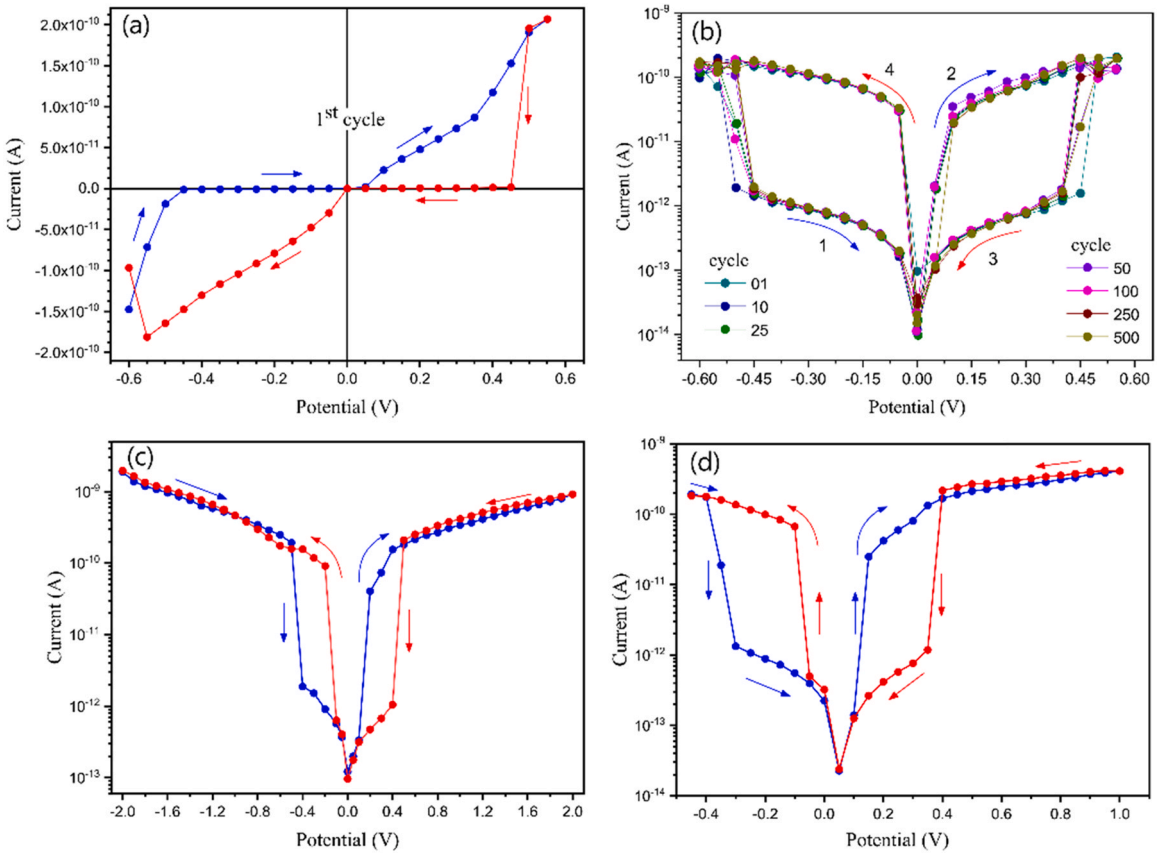

Fig. 5. (a) I–V curve of the PW layer obtained with an Rh pointed head spring probe as the top electrode and an Au film as the bottom electrode. (b) Semi-log plot of the current versus voltage with cycles 1st, 10th, 25th, 50th, 100th, 200th, and 500th superimposed. I-V semi-log curves for the 1st cycle obtained under different maximum voltages and symmetric (c) and asymmetric loops (d). The arrows indicate how the cycle was traversed by voltage.

voltages. Fig. 5(c) and (d) displays two semi-log I-V curves with symmetric and asymmetric maximum voltages, respectively. The abnormal bipolar RS was observed with similar LRS/HRS switching ratios and no dependence on the voltage sequence or maximum voltage was observed.

In Fig. 6(a), we are showing the retention of the LRS and HRS states for times as long as 1000 s. The LRS and HRS were achieved by applying voltage pulses at + 0.2 V and − 0.4 V, respectively. The retention measurements were carried out after the device was submitted to 250 switching cycles. The HRS and LRS states remain stable with a small increase in resistance after 400 s. The RS ratio [R_{HRS}/R_{LRS}] remained constant at 2 orders of magnitude up to 1000 s Fig. 6(b) describes the conduction mechanisms for the 1st cycle on a log-log scale. The LRS state shows two slopes, 1.1 for lower voltages and 1.9 close to the reset point. After the switching to the HRS state, a 0.9 slope is observed for lower voltages. Similar slopes are observed for the 500th cycle confirming the stability of the system, as shown on the right side of Fig. 6(b). Slopes close to 1 are associated

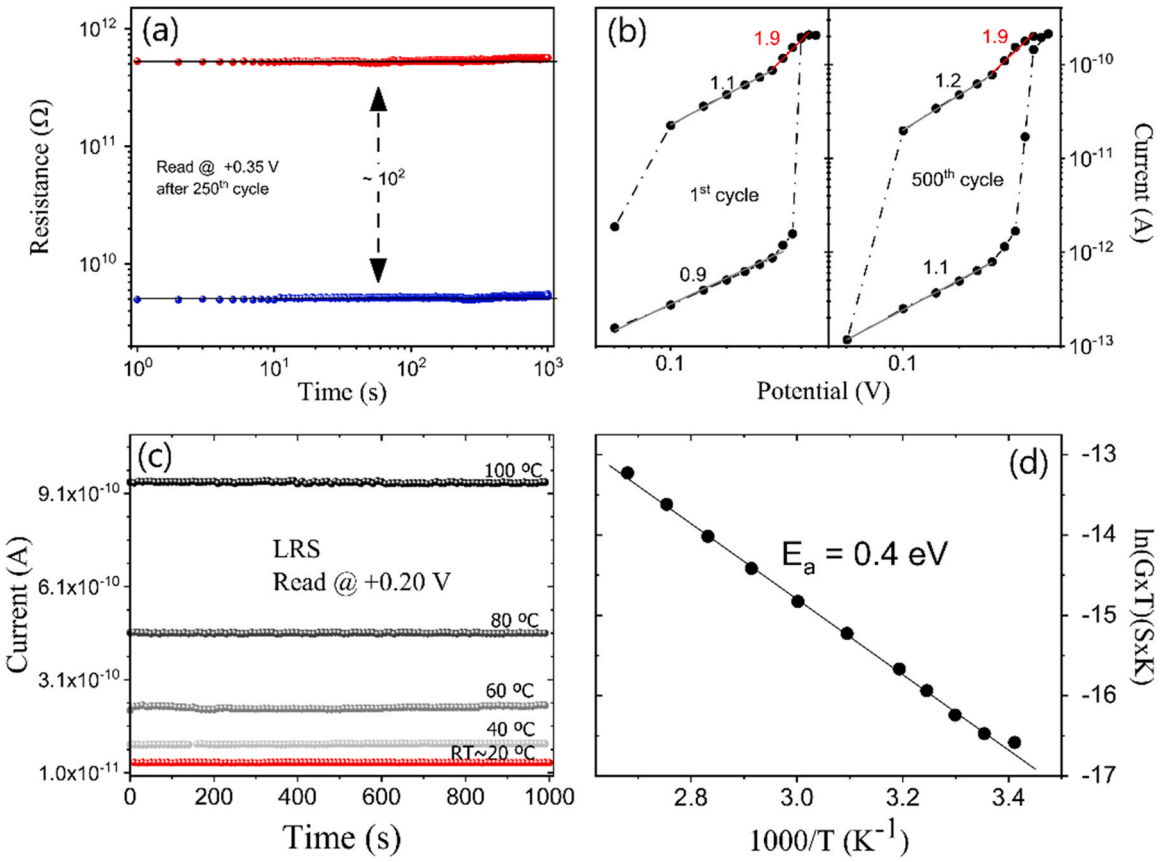

Fig. 6. (a) Retention of the resistance LRS and HRS states measured as a function of time. (b) Log-log plots of the I – V curves in the positive bias region for 1st and 500th cycles, respectively. (c) LRS state at different temperatures as a function of time and read at + 0.20 V. (d) Plot of the product of conductance and temperature versus the reciprocal temperature.

with the ohmic law and close to 2 to space charge limited current (SCLC) mechanism. The Ohmic conduction behavior ($I \propto V$) is observed up to ~ 0.4 V and the quadratic term of Child's Law [40]. close to the reset point in the LRS state.

Fig. 6(c) shows the LRS state as a function of time for different temperatures in the interval from room temperature up to 100 ºC. The LRS was set and kept on at a constant potential of + 0.2 V while the current was read up to 1000 s for each temperature. The current was very stable with time and increased exponentially with the temperature. From the Arrhenius plot in Fig. 6(d), we see that the product of conductance and temperature (GxT) depends linearly on the reciprocal temperature, which is typical of ionic conduction. The calculated activation energy of 0.4 eV is similar to values obtained for Prussian Blue analogs under controlled humidity, i. e., 0.48 eV for $Co^{II}[Cr^{III}(CN)_6]_{2/3}.nH_2O$ with 28% relative humidity [41] and 0.37 eV for $Cu^{II}[Fe^{III}(CN)_6]_{2/3}\cdot nH_2O$ with 90% relative humidity [42]. These activation energies were associated with ionic conduction by the proton hopping mechanism. Ohkoshi et al. [41] considered negligible the contribution of alkali cations to the ionic conduction since their samples do not contain these elements and Hosseini et al. [42] ruled out the possibility of potassium ions as a possible conduction pathway based on the relatively low observed value of activation energy considering the necessity of charge neutrality and the size of the ion.

Taking into account the superficial concentration of potassium observed by XPS at the surface and the presence of grain boundaries along with the thickness of the layers as can be seen in the STEM cross-section images, we could consider that the ionic conduction in PW layers occurs by potassium hopping at the grain boundaries that requires lower activation energies than migration in the intrinsic material. The ohmic and SCLC conduction mechanisms could then be explained by the migration of K^+ under the applied potential reducing or decreasing the amount of these ions at the Rh/PW and PW/Au interfaces, as observed for ions and vacancies in oxide layers [10,14,19]. Also, the abnormal RS curves are symmetric for positive and negative bias, which implies the same switching mechanism for both polarities. If the applied potential is small, the migration of ions is low, and the conduction is ohmic. For higher potentials and close to the reset voltages, the K ions migrate to one of the interfaces Rh/PW or PW/Au, depending on the polarity, and on one side there will be accumulation and on the other one depletion. The depletion region is noted by the SCLC conduction that controls the ion transport with the increase of the applied voltage.

4. Conclusions

We have observed the abnormal resistive switching in uniform and homogeneous Prussian White layers electrodeposited on Au thin films. The ON/OFF ratio was of about 2 orders of magnitude and the switching was reproducible for consecutive 500 cycles with retention of HRS and LRS measured up to 1000 s. The ionic conduction with an activation energy of 0.4 eV due to the hopping of ions, possibly potassium at grain boundaries, was observed.

CRediT authorship contribution statement

F.L. Faita, L.B. Avila, C.C. Plá Cid, and A.A. Pasa were responsible for the preparation of the samples. F.L. Faita, J.P.B. Silva, M.H. Boratto, C.F.O. Graeff, M.J.M. Gomes, C.C. Plá Cid, C.K. Müller, and A.A. Pasa were responsible for the different measurements done to

characterize the samples. A.A. Pasa, C.K. Müller and F.L. Faita were responsible for generating the final version of the manuscript.

Declaration of Competing Interest

The authors declare that they have no known competing financial interests or personal relationships that could have appeared to influence the work reported in this paper.

Acknowledgments

The authors acknowledge TESCAN, Zeiss, and WITec for assistance during electron microscopy and Raman imaging of the samples and LCME/UFSC for the EDS measurements (LCME-MAT-2021). We thank D. Hildebrand for his technical assistance. This research was supported by the funding agencies: CNPQ, FINEP, CAPES (finance code 001), DAAD (project 249302), FAPESP (process 2013/07296, 2017/20809-0, 2020/04721-8), and the Portuguese Foundation for Science and Technology (FCT) in the framework of the Strategic Funding Contract UIDB/ 04650/2020.

References

[1] A. Chen, A review of emerging non-volatile memory (NVM) technologies and applications, Solid State Electron. 125 (2016) 25–38, https://doi.org/10.1016/j.sse.2016.07.006
[2] D. Ielmini, H.S.P. Wong, In-memory computing with resistive switching devices, Nat. Electron. 1 (2018) 333–343, https://doi.org/10.1038/s41928-018-0092-2
[3] S. Slesazeck, T. Mikolajick, Nanoscale resistive switching memory devices: a review, Nanotechnology 30 (2019) 352003, https://doi.org/10.1088/1361-6528/ab2084
[4] S. Siegel, C. Baeumer, A. Gutsche, M. von Witzleben, R. Waser, S. Menzel, R. Dittmann, Trade-off between data retention and switching speed in resistive switching ReRAM devices, Adv. Electron. Mater. 7 (2021), https://doi.org/10.1002/aelm.202000815
[5] S. Gaba, P. Sheridan, J. Zhou, S. Choi, W. Lu, Stochastic memristive devices for computing and neuromorphic applications, Nanoscale 5 (2013) 5872–5878, https://doi.org/10.1039/c3nr01176c
[6] M. Prezioso, F. Merrikh-Bayat, B.D. Hoskins, G.C. Adam, K.K. Likharev, D.B. Strukov, Training and operation of an integrated neuromorphic network based on metal-oxide memristors, Nature 521 (2015) 61–64, https://doi.org/10.1038/nature14441
[7] J. Xiong, R. Yang, J. Shaibo, H.M. Huang, H.K. He, W. Zhou, X. Guo, Bienenstock, Cooper, and Munro learning rules realized in second-order memristors with tunable forgetting rate, Adv. Funct. Mater. 29 (2019) 1807316, https://doi.org/10.1002/adfm.201807316
[8] A. Sawa, Resistive switching in transition metal oxides, Mater. Today 11 (2008) 28–36, https://doi.org/10.1016/S1369-7021(08)70119-6
[9] S.A. Mojarad, J.P. Goss, K.S.K. Kwa, P.K. Petrov, B. Zou, N. Alford, A. O'Neill, Anomalous resistive switching phenomenon, J. Appl. Phys. 112 (2012) 124516, https://doi.org/10.1063/1.4770489
[10] D.S. Jeong, H. Schroeder, R. Waser, Abnormal bipolar-like resistance change behavior induced by symmetric electroforming in Pt/TiO2/Pt resistive switching cells, Nanotechnology 20 (2009) 375201, https://doi.org/10.1088/0957-4484/20/37/375201
[11] A. Shih, W. Zhou, J. Qiu, H.J. Yang, S. Chen, Z. Mi, I. Shih, Highly stable resistive switching on monocrystalline ZnO, Nanotechnology 21 (2010) 125201, https://doi.org/10.1088/0957-4484/21/12/125201
[12] J. Sun, C.H. Jia, G.Q. Li, W.F. Zhang, Control of normal and abnormal bipolar resistive switching by interface junction on In/Nb:SrTiO3 interface, Appl. Phys. Lett. 101 (2012) 2012–2015, https://doi.org/10.1063/1.4755842
[13] D.Y. Guo, Z.P. Wu, L.J. Zhang, T. Yang, Q.R. Hu, M. Lei, P.G. Li, L.H. Li, W.H. Tang, Abnormal bipolar resistive switching behavior in a Pt/GaO1.3/Pt structure, Appl. Phys. Lett. 107 (2015) 32104, https://doi.org/10.1063/1.4927332
[14] G. Wang, C. Li, Y. Chen, Y. Xia, D. Wu, Q. Xu, Reversible voltage dependent transition of abnormal and normal bipolar resistive switching, Sci. Rep. 6 (2016) 36953, https://doi.org/10.1038/srep36953
[15] U. Tu Thi Doan, A. Tuan Thanh Pham, T.B. Phan, S. Park, A.T. Luu, Q.H. Nguyen, T.S. Lo, T.D. Tap, M. Ohtani, N.K. Pham, Abnormal volatile and normal stable bipolar resistive switching characteristics of hybrid nanocomposites: morphology–defects–property 'Relationship, J. Alloy. Compd. 857 (2021) 157602, https://doi.org/10.1016/j.jallcom.2020.157602
[16] J. Yoo, J. Woo, J. Song, H. Hwang, Threshold switching behavior of Ag-Si based selector device and hydrogen doping effect on its characteristics, AIP Adv. 5 (2015) 127221, https://doi.org/10.1109/JEDS.2018.2836400
[17] Y.J. Huang, S.C. Chao, D.H. Lien, C.Y. Wen, J.H. He, S.C. Lee, Dual-functional memory and threshold resistive switching based on the push-pull mechanism of oxygen ions, Sci. Rep. 6 (2016) 23954, https://doi.org/10.1038/srep23945
[18] J. Resende, A. Sekkat, V.H. Nguyen, T. Chatin, C. Jiménez, M. Burriel, D. Bellet, D. Muñoz-Rojas, Planar and transparent memristive devices based on titanium oxide coated silver nanowire networks with tunable switching voltage, Small 17 (2021) 2007344, https://doi.org/10.1002/smll.202007344
[19] F. Nardi, S. Balatti, S. Larentis, D.C. Gilmer, D. Ielmini, Complementary switching in oxide-based bipolar resistive-switching random memory, IEEE Trans. Electron. Devices 60 (2013) 70–77, https://doi.org/10.1109/TED.2012.2226728
[20] A. Siemon, T. Breuer, N. Aslam, S. Ferch, W. Kim, J. Van Den Hurk, V. Rana, S. Hoffmann-Eifert, R. Waser, S. Menzel, E. Linn, Realization of Boolean logic functionality using redox-based memristive devices, Adv. Funct. Mater. 25 (2015) 6414–6423, https://doi.org/10.1002/adfm.201500865
[21] J. Zhao, S. Li, W. Tong, G. Chen, Y. Xiao, S. Lei, B. Cheng, Light-induced anomalous resistive switches based on individual organic–inorganic halide perovskite micro-/nanofibers, Adv. Electron. Mater. 4 (2018) 1800206, https://doi.org/10.1002/aelm.201800206
[22] L. Wang, J. Song, R. Qiao, L.A. Wray, M.A. Hossain, Y.-D. Chuang, W. Yang, Y. Lu, S. Kakimoto, J.-J. Lee, J.B. Goodenough, S. Vail, D. Evans, X. Zhao, M. Nishijima, Rhombohedral Prussian white as cathode for rechargeable sodium-ion batteries, J. Am. Chem. Soc. 137 (2015) 2548–2554, https://doi.org/10.1021/ja510347s
[23] M.J. Piernas-Muñoz, E. Castillo-Martínez, O. Bondarchuk, M. Armand, T. Rojo, Higher voltage plateau cubic Prussian White for Na-ion batteries, J. Power Sources 324 (2016) 766–773, https://doi.org/10.1016/j.jpowsour.2016.05.050
[24] G. He, L.F. Nazar, Crystallite size control of prussian white analogues for nonaqueous potassium-ion batteries, ACS Energy Lett. 2 (2017) 1122–1127, https://doi.org/10.1021/acsenergylett.7b00179
[25] W.R. Brant, R. Mogensen, S. Colbin, D.O. Ojwang, S. Schmid, L. Häggström, T. Ericsson, A. Jaworski, A.J. Pell, R. Younesi, Selective control of composition in Prussian white for enhanced material properties, Chem. Mater. 31 (2019) 7203–7211, https://doi.org/10.1021/acs.chemmater.9b01494
[26] C.Q.X. Lim, Z.K. Tan, Prussian white with near-maximum specific capacity in sodium-ion batteries, ACS Appl. Energy Mater. 4 (2021) 6214–6220, https://doi.org/10.1021/acsaem.1c00987
[27] B.F. Baggio, C. Vicente, S. Pelegrini, C.C. Plá Cid, I.S. Brandt, M.A. Tumelero, A.A. Pasa, Morphology and structure of electrodeposited Prussian Blue and Prussian White thin films, Materials 12 (2019) 1103, https://doi.org/10.3390/ma12071103
[28] E. Linn, R. Rosezin, C. Kügeler, R. Waser, Complementary resistive switches for passive nanocrossbar memories, Nat. Mater. 9 (2010) 403–406, https://doi.org/10.1038/nmat2748
[29] P. Zhang, W. Zhai, Z. Yan, X. Li, Y. Li, S. Zheng, Y. Tang, L. Lin, J.M. Liu, High-performance complementary resistive switching in ferroelectric film, AIP Adv. 11 (2021) 065202, https://doi.org/10.1063/5.0043536
[30] L.B. Avila, C.K. Müller, D. Hildebrand, F.L. Faita, B.F. Baggio, C.C. Plácid, A.A. Pasa, Resistive switching in electrodeposited Prussian blue layers, Materials 13 (2020) 5618, https://doi.org/10.3390/ma13245618
[31] M.F. Alamini, R.C. da Silva, V.C. Zoldan, E.A. Isoppo, U.P. Rodrigues Filho, F.D.A. Aarão Reis, A.N. Klein, A.A. Pasa, Normal versus anomalous roughening in electrodeposited Prussian Blue layers, Electrochem. Commun. 13 (2011) 1455–1458, https://doi.org/10.1016/j.elecom.2011.09.025
[32] C.D. Wanger, W.M. Riggs, L.E. Davis, J.F. Moulder, L.E. Muilenberg, Handbook of X-ray Photoelectron Spectroscopy, 1979.
[33] E. Reguera, J.F. Bertrán, C. Diaz, J. Blanco, S. Rondón, Mössbauer and infrared spectroscopic studies of novel mixed valence states in cobaltous ferrocyanides and ferricyanides, Hyperfine Interact. 53 (1990) 391–395, https://doi.org/10.1007/BF02101072
[34] O. Sato, Y. Einaga, A. Fujishima, K. Hashimoto, Photoinduced long-range magnetic ordering of a cobalt - iron cyanide, Inorg. Chem. (1999) 4405–4412.
[35] N. Shimamoto, S.I. Ohkoshi, O. Sato, K. Hashimoto, Control of charge-transfer-induced spin transition temperature on cobalt-iron Prussian blue analogues, Inorg. Chem. 41 (2002) 678–684, https://doi.org/10.1021/ic010915u
[36] A. Bleuzen, C. Lomenech, V. Escax, F. Villain, F. Varret, C. Cartier Dit Moulin, M. Verdaguer, Photoinduced ferrimagnetic systems in Prussian blue analogues CIxCo4[Fe(Cn)6]y (Ci = alkali cation). 1. Conditions to observe the phenomenon, J. Am. Chem. Soc. 122 (2000) 6648–6652, https://doi.org/10.1021/ja000348u
[37] G. Moretti, C. Gervais, Raman spectroscopy of the photosensitive pigment Prussian blue, J. Raman Spectrosc. 49 (2018) 1198–1204, https://doi.org/10.1002/jrs.5366
[38] R. Mažeikiene, G. Niaura, A. Malinauskas, Electrochemical redox processes at cobalt hexacyanoferrate modified electrodes: an in situ Raman spectroelectrochemical study, J. Electroanal. Chem. 719 (2014) 60–71, https://doi.org/10.1016/j.jelechem.2014.02.012
[39] L. Chua, If it ' s pinched it ' s a memristor, 2014. https://doi.org/10.1088/0268–1242/29/10/104001.
[40] M.A. Lampert, Simplified theory of space-charge-limited currents in an insulator with traps, Phys. Rev. 103 (1956) 1648–1656, https://doi.org/10.1103/PhysRev.103.1648
[41] S.I. Ohkoshi, K. Nakagawa, K. Tomono, K. Imoto, Y. Tsunobuchi, H. Tokoro, High proton conductivity in prussian blue analogues and the interference effect by magnetic ordering, J. Am. Chem. Soc. 132 (2010) 6620–6621, https://doi.org/10.1021/ja100385f
[42] P. Hosseini, K. Wolkersdörfer, M. Wark, E. Redel, H. Baumgart, G. Wittstock, Morphology and conductivity of copper hexacyanoferrate films, J. Phys. Chem. C 124 (2020) 16849–16859, https://doi.org/10.1021/acs.jpcc.0c06114